



Nonlinear viscoelasticity of fat crystal networks

Braulio A. Macias-Rodriguez¹ · Randy H. Ewoldt² · Alejandro G. Marangoni¹

Received: 20 July 2017 / Revised: 1 January 2018 / Accepted: 14 January 2018 / Published online: 12 February 2018
© Springer-Verlag GmbH Germany, part of Springer Nature 2018

Abstract

The rheology of fat crystal networks under linear shear deformations has been extensively studied due to its role in material functionality and sensory perceptions. In contrast, there has been limited focus on their viscoelastic response under large shear deformations imposed during processing and product use. We probed the nonlinear viscoelastic behavior of fats displaying mechanics akin to ductile and brittle solids using large amplitude oscillatory shear (LAOS). Using the FT-Chebyshev stress decomposition method, and local measures of nonlinear viscoelasticity, we obtained rheological properties relevant to bulk behavior. We found that ductile fats dissipate more viscous energy than brittle fats and show increased plastic deformation. Structural characterization revealed the presence of three hierarchy levels and layered microstructures in ductile fats in contrast to only two hierarchies and random microstructures in brittle fats. We suggest that these structural features account for increased hypothesize dissipation, which contributes to their ductile-like macroscopic behavior.

Keywords Fat · Ductile · Brittle · Rheology · Nonlinear

Introduction

Fats such as shortening, butter, and margarine are an example of polycrystalline pasty materials composed of an interacting continuous network at particle concentrations above the critical volume fraction ($\phi_c \approx 0.05$ – 0.10) and a liquid phase contained within (Marangoni et al. 2012). The essential role of fats in foods (e.g., lubrication, texture), and the consumer health-driven trend towards low saturates and no-*trans* foods due to the association of “bad fats” with cardiovascular diseases, has led to increased interest in these systems (Uauy et al. 2009; Vartiainen et al. 2010; Marangoni et al. 2012). From a mechanical perspective, fats resemble flocculated colloidal gels with the magnitude of the elastic modulus depending on the microscopic crystal network and its structural heterogeneity (van den

Tempel 1961; Narine and Marangoni 1999a). This structural organization allows fats to sustain stress or deformation up to a certain limit, beyond which they yield and irreversibly deform displaying some intriguing nonlinear rheological phenomena. Some of these rheological features include yielding, shear thinning, intracycle strain stiffening, and thixotropy (Scott Blair 1954; Sone 1961; Haighton 1965; Thareja 2013; Macias-Rodriguez and Marangoni 2016a).

The rheological properties of fats are a consequence of their remarkably complex hierarchical organization, showcasing structural building blocks spanning from the molecular to the microworld, and their physical interactions (Narine and Marangoni 1999b; Marangoni et al. 2012). Nanoplatelets (the fundamental ‘crystal unit’) arise from the epitaxial stacking of crystal lamellae which in turn are made up by TAG molecules stacked longitudinally and side by side following a specific subcell unit arrangement (α , β' , β). Nanoplatelets self-assemble into large fractal clusters or aggregates via diffusion-limited cluster aggregation (DLCA) and reaction-limited cluster aggregation (RLCA) to form a space-filling microscopic gel-like network (Narine and Marangoni 1999a; Peyronel et al. 2014a). The network is held together by van der Waals forces or short-range attractive interactions and presents a variety of morphologies (e.g., spherulitic, needle-like, grain-like) which offers equal variety in the mechanics of deformation (Heertje 1993).

Electronic supplementary material The online version of this article (<https://doi.org/10.1007/s00397-018-1072-1>) contains supplementary material, which is available to authorized users.

✉ Alejandro G. Marangoni
amarango@uoguelph.ca

¹ Department of Food Science, University of Guelph, Guelph, ON N1G 2W1, Canada

² Department of Mechanical Science and Engineering, University of Illinois at Urbana-Champaign, Urbana, IL 61801, USA

A number of studies have sought to establish rheology-structure relationships in fat crystal networks. Major progress has been made on understanding fat linear viscoelasticity, and its role on macroscopic mechanical functionality. By functionality or performance, we refer to the range of textural viscoelastic attributes that make fats suited for specific applications (e.g., firmness, spreadability). Fat linear viscoelasticity concepts have been developed based on fractal theories (originally proposed for colloidal gels), according to which the elastic modulus scales in a power law fashion with particle volume fraction $G' \sim \gamma\phi^n$, where n is related to the compactness of the individual clusters or mass fractal dimension (D) and γ is a proportionality constant dependent on the size and the interactions of primary particles (Narine and Marangoni 1999a, c). For most complex fat systems ($\phi > 0.1$), the weak link regime dominates, e.g., the elasticity of the network is given by the interfloc links rather than the fractal flocs (Narine and Marangoni 1999a, c). Given the complexities imposed by the multiple physical length scales of fats, developing rigorous relationships among interparticle forces, structure, and rheology remains a challenging problem.

While there has been much focus on fats' mechanical response in the linear regime, there has been limited attention on their nonlinear regime—that is, at large deformations (Macias-Rodriguez and Marangoni 2016a, 2017; Macias-Rodriguez et al. 2017). During application processes and final product use, fats are subjected to substantial deformations well beyond their onset of nonlinear behavior ($\gamma_c \approx 0.03\%$, $\tau_c = 50\text{--}500$ Pa) (Macias-Rodriguez and Marangoni 2016a). For instance, extrusion and rolling, processes akin to cold working of metals (forging), induce plastic deformation to shape bulk fat into micron-sized thin films by imposing nonlinear rates of deformation in the order of $1\text{--}100$ s⁻¹ and pressures of up to 50 kPa (Marangoni et al. 2012). In a broader context, the nonlinear behavior of a variety of colloidal gels and soft solid food gels has been studied in much detail using large amplitude oscillatory shear (LAOS) rheology. Unlike step input tests (e.g., creep compliance, stress relaxation, start-up of steady shear), oscillatory shear tests (i) gradually lead up to yield, (ii) can decompose energy storage and loss mechanisms, and (iii) have a better signal-to-noise ratio for comparing between materials (since oscillations lock-in on each frequency probed). Yielding under LAOS has been attributed to fatigue-induced fluidization in attractive carbon black gels (Gibaud et al. 2016), breakdown from large to gradually smaller structural length scales far above the primary particle size in concentrated colloidal gels (Kim et al. 2014), microstructural anisotropy in thermo-reversible nanoparticle gels (Min Kim et al. 2014), and microcrack nucleation and propagation in soft solid gels (Faber et al. 2017).

In previous research reports, we described the nonlinear rheological behavior of fats as related to their functionality (Macias-Rodriguez and Marangoni 2016a, 2017; Macias-Rodriguez et al. 2017). Analysis of the nonlinear response

using Fourier transform (FT) rheology and Lissajous-Bowditch curves indicated different material behavior depending on the intended use of fat materials, e.g., third harmonic spectra and Lissajous-Bowditch curves suggested superior ability of roll-in shortenings to withstand larger deformations and less intracycle strain stiffening. Additionally, stress decomposition using Chebyshev polynomials suggested that fats share similar elastic properties but different viscous properties depending on their end functionality. In this work, we further studied the yielding behavior of two sets of materials: roll-in and all-purpose shortenings, which share mechanical responses similar to brittle and ductile solids. We determine phenomenological rheological differences among these materials under LAOS deformations (an idealized version of the in-use flow conditions), which we correlate to their observed macroscopic behavior and structural properties.

Experimental

Sample preparation

Bulk composition and linear elastic moduli of the samples used in this study are described in Table 1. All samples show weak frequency dependence with $G' > G''$ (see supplementary material Fig. A7), a typical behavior typical of fats. For a detailed description on the molecular composition and other physico-chemical properties of the samples studied herein, refer to Macias-Rodriguez and Marangoni (2016b). All samples had intermediate volume fraction ($\phi_{16\text{ }^\circ\text{C}} \approx 0.2\text{--}0.3$) and were of commercial origin as their physico-chemical properties cannot be easily replicated in a bench scale, and hence represent “real” materials (Macias-Rodriguez and Marangoni 2016a). The only exception was sample D2 which was formulated and crystallized in house as described elsewhere (Acevedo and Marangoni 2013). It is noteworthy that brittle and ductile rheological behavior cannot be explained by differences in volume fraction as demonstrated in our previous study (Macias-Rodriguez and Marangoni, 2016a, b). Although exact material processing conditions of D1, B1, and B2 are unknown, it can be inferred that brittleness is imparted via static crystallization where crystal growth is promoted over nucleation, while ductility or “plasticity” is obtained from dynamic crystallization, high degree of cooling, and mechanical working, where crystal nucleation is favored and crystal growth is delayed (Acevedo and Marangoni 2013). Differences in rheological behavior cannot be attributed.

Prior to rheological characterization, samples were carefully prepared in the form of cylinders of 30-mm diameter using a hollow steel cylinder and stored at 16 °C overnight to allow for reformation of fractured bonds or local damage induced by cutting and to remove residual stresses. Cutting was

Table 1 Fat functionality and bulk composition for each material class, linear elastic moduli, and maximum stress at rupture or fracture at $\omega = 3.6 \text{ rad s}^{-1}$ and $\gamma_0 = 0.01\%$

Sample	Composition	$G'_{LVE} (\times 10^6)$	τ_{yield}
D1	Roll-in nonhydrogenated canola oil, modified palm, and palm kernel oils	2.1 ± 0.2	3964.8 ± 102.1
D2 ^a	Roll-in fully hydrogenated soybean oil, soybean oil, and glycerol monopalmitate	2.1 ± 0.3	4464.4 ± 117.9
B1	All-purpose nonhydrogenated palm oil and modified palm oil	4.7 ± 0.8	4874.7 ± 61.1
B2	All-purpose soybean oil interesterified	1.8 ± 0.1	3071.9 ± 151.6

^a Sample was formulated and crystallized in-house

performed using a wire lubricated with mineral oil to minimize flaw or crack formation that may act as points of stress concentration leading to premature failure.

Rheometry

Samples were carefully transferred onto the lower plate of a rotational rheometer (MCR 302, Anton Paar) and loaded within a parallel plate geometry using $3 \pm 0.5 \text{ N}$ axial force to avoid the formation of new microstructures and ensure reproducible results (Macias-Rodriguez and Marangoni 2016a). It has been shown that overloading modifies the rheology, i.e., it reduces the critical strain and critical stress and causes a right shift of the “flow” point $G' = G''$, and the microstructure of fat crystal networks (Heertje et al. 1988). After loading, samples were allowed to relax the axial force to a constant value over a zero strain relaxation test for at least 15 min, being equilibrated at $16 \text{ }^\circ\text{C}$. This temperature was chosen to resemble thermal conditioning during rolling and layering of fats (Macias-Rodriguez and Marangoni 2016a). Temperature was controlled using Peltier units located in the lower plate and the hood of the rheometer. All experiments were performed with parallel plate geometries. Compression tests were performed with parallel plates (DIA = 50 mm) lubricated with a thin layer of mineral oil to reduce friction at the boundaries. Shear oscillatory tests were performed with parallel plates (DIA = 20 mm) modified with filter paper (Whatman grade 5, GE Healthcare Life Sciences) attached to the top and bottom plates to improve sample adhesion to contacting boundaries and minimize wall slip during measurements (see modified geometry in supplementary material Fig. A1). Parallel plate geometries were selected despite its heterogeneous shear rate field, as it allows for loading of preformed samples.

Small amplitude and large amplitude oscillatory shear experiments (SAOS, LAOS) were performed in strain-controlled mode on the combined motor-transducer rheometer. Tests involved strain sweeps from the linear region until post-yielding of the material ($\gamma_0 = 0.001\text{--}100\%$) with frequency of $\omega = 3.6 \text{ rad s}^{-1}$ representative of the rolling process ($\omega \approx 2\text{--}7 \text{ rad s}^{-1}$) (Chakrabarti-Bell et al. 2010). Strains γ_0 and stresses τ represent bulk apparent responses (i.e. when measuring points do not overlap at different gaps (e.g. after failure). However, the stress at the rim of the plate can be treated as true.

LAOS analysis

Beyond the linear viscoelastic region, at large input amplitudes, complex nonlinear phenomena manifest in the oscillatory stress response as nonsinusoidal waves with higher order harmonic contributions. If represented via Lissajous-Bowditch (L-B) curves, parametric plots of stress versus strain or strain rate, nonlinearity causes deviation from an elliptical shape of the response. Consequently, the conventional interpretation of the elastic and viscous moduli in the theory of linear viscoelasticity is no longer applicable. Various frameworks have been developed to interpret nonlinear contributions including Fourier transform (FT) rheology, FT-Chebyshev stress decomposition, and the sequence of physical processes (SPP) (Cho et al. 2005; Ewoldt et al. 2008; Hyun et al. 2011; Rogers 2012). Despite the utility of the latter approach (recently applied to yielding of a heterogeneous colloidal gel), we refrain from using time-dependent dynamic moduli R' and R'' as these measures are inherently highly dimensional (Rogers 2012). Instead, we use FT-Chebyshev stress decomposition method as it provides meaningful low-dimensional metrics that successfully simplify the complex nonlinear rheological phenomena of the materials fats investigated here.

In the stress decomposition framework, the total stress is represented as a superposition of the so-called elastic τ' and viscous stresses τ'' using symmetry arguments (Cho et al. 2005). The symmetry arguments are mathematically well defined, so long as shear symmetry is maintained. We note that in extreme cases, such as discontinuous constitutive equations with yield, the decomposed stresses may mix elastic and viscous effects at very large amplitudes) (Rogers and Lettinga 2012). The elastic and viscous stresses are then unambiguously described by a set of orthogonal Chebyshev polynomials of the first kind, as proposed by Ewoldt et al. (2008):

$$\tau'(x) = \gamma_0 \sum_{n:\text{odd}} e_n(\omega, \gamma_0) T_n(x), \quad (1)$$

$$\tau''(y) = \dot{\gamma}_0 \sum_{n:\text{odd}} v_n(\omega, \gamma_0) T_n(y), \quad (2)$$

where $T_n(x)$ and $T_n(y)$ corresponds to n th order of the Chebyshev basis functions, $x = \gamma(t)/\gamma_0$ and $y = \dot{\gamma}(t)/\dot{\gamma}_0$, with γ_0 and $\dot{\gamma}_0$ being the maximum in-cycle strain and shear rate, and $e_n(\omega, \gamma_0)$ and $v_n(\omega, \gamma_0)$ refer to the elastic and viscous Chebyshev coefficients of order n . The Chebyshev coefficients are directly related to the higher order Fourier coefficients in the time domain as $e_n = G'_n(-1)^{(n-1)}/2$ and $v^n = G''_n/\omega = \eta'_n$, respectively. Note that even harmonic ($n = \text{even}$) Fourier and Chebyshev harmonic/coefficients are neglected as they are associated with broken shear symmetry, e.g., with responses that have not yet reached the time periodic state. It is worth noting that even harmonics are *not* related to wall slip in general (Ewoldt et al. 2010). They are commonly mistaken as such in the literature, but the only slip-related even harmonics are those associated with broken shear symmetry, such as “dynamic” wall slip that inhibits steady state (Graham 1995). Just as the third-order Fourier harmonic, the third-order Chebyshev basis function signals depart from linearity and additionally provide physical meaning to the stress response. It is important to emphasize that linear material functions G' and G'' (equivalent to G'_1 and G''_1) represent average stress responses equivalent to first-order Chebyshev coefficients e_1 and v_1 . Instead, third and higher order Chebyshev coefficients capture uniquely local responses in the distorted stress signal (i.e., bent, twisted L-B curves). Specifically, the signs of the leading order elastic and viscous Chebyshev coefficients e_3 and v_3 reveal the underlying cause driving average changes in the elastic and viscous intercycle stress response. For example, for G'_1 decreasing, and $e_3 > 0$, large instantaneous strain rates are responsible for the average elastic softening. In the same way, for G''_1 decreasing and $v_3 < 0$, large instantaneous strain rates also drive average viscous thinning. For a full description on how to interpret the leading order Chebyshev LAOS strain nonlinearities for yielding materials, refer to Ewoldt and Bharadwaj (2013), who updated the physical interpretation of Ewoldt et al. (2008).

Separate from the stress decomposition framework, we will find great value in using the local measures for yielding materials under LAOS as recently updated by Ewoldt and Bharadwaj (2013), which can be interpreted geometrically from L-B curves. Metrics of elastic energy storage and viscous energy dissipation can be determined from characteristic points during the oscillation (at extreme values of strain and strain rate) as

$$G'_M \equiv \frac{d\tau}{d\gamma} \Big|_{\gamma=0} = \sum_{n:\text{odd}} n G'_n = e_1 - 3e_3 + \dots, \quad (3)$$

$$G'_L \equiv \frac{\tau}{\gamma} \Big|_{\gamma=\pm\gamma_0} = \sum_{n:\text{odd}} G'_n (-1)^{(n-1)/2} = e_1 + e_3 + \dots, \quad (4)$$

$$\eta'_M \equiv \frac{d\tau}{d\dot{\gamma}} \Big|_{\dot{\gamma}=0} = \frac{1}{\omega} \sum_{n:\text{odd}} n G''_n (-1)^{(n-1)/2} = v_1 - 3v_3 + \dots, \quad (5)$$

$$\eta'_L \equiv \frac{\tau}{\dot{\gamma}} \Big|_{\dot{\gamma}=\pm\dot{\gamma}_0} = \frac{1}{\omega} \sum_{n:\text{odd}} G''_n = v_1 + v_3 + \dots, \quad (6)$$

where G'_M is the minimum strain or tangent modulus at $\gamma_0 = 0$ and G'_L is the large strain or secant modulus at $\gamma_0 = \gamma_{\text{max}}$. Likewise, η'_M is the minimum rate viscosity and η'_L is the large rate viscosity. These deliberately chosen material functions reduce to G'_1 and G''_1 ($\eta'_1 = G''/\omega$) in the linear regime.

Data collection and processing

For LAOS analysis, raw strain-stress data were collected at a sampling rate of 512 points per oscillatory cycle. Due to the thixotropic nature of our samples, 25 oscillatory cycles were applied to enable material adaptation to each new deformation (i.e., allow initial transient responses to die out) while also avoiding over-softening of the sample due to shearing (see supplementary material: Figs. A2–A3 to visualize the time evolution of the first harmonic moduli and the effect of pre-oscillations on material response and Fig. A4 for acquired raw elastic Lissajous-Bowditch curves at selected strain values for all samples). The application of pre-oscillations leads to have similar qualitative behavior, i.e., they do not change the ductile and brittle rheological behavior of the investigated materials (see Figs. A2–A3). It is important to note treating LAOS nonlinearities in a steady state, where LAOS may induce certain structural change and inevitably affect the time-dependent yielding response. This and other relevant limitations inherent to LAOS are discussed at length by Li et al. (2009). Recently, Moghimi et al. (2017) also demonstrated that pre-shearing at large amplitudes tunes the yielding process of colloidal gels. Typically, the last three to five waveforms at each coordinate pair $\{\omega, \gamma_0\}$ were input to a custom-written MATLAB code (Ewoldt et al. 2009). The software processes the signal with a discrete Fourier transform, calculates relevant measures of nonlinear viscoelasticity, and smoothes and reconstructs the stress signal by allowing only odd, integer harmonic components, up to a cutoff such that $I_n/I_1 \geq 0.05$ to avoid noise. Filter performance for selected deformations has been included in supplementary material (Fig. A5). Overall, the multiple waveform collection and post-processing provides greater accuracy and increased signal to noise (S/N) ratio and removes random noise obscuring any real material response (Ewoldt et al. 2009). To further minimize the effect of shear artifacts (instabilities, slip, edge fracture) on the LAOS data, we constrained our LAOS analysis to $\gamma_0 \leq 10\%$ as experimental error increased at larger strains and severe slip was even visually observed at $\gamma_0 \approx 30\%$ and beyond. Although the maximum shear rates resulting from these analysis $\dot{\gamma}_0 \approx 1 \text{ s}^{-1}$ are comparatively low to those imposed during industrial rolling conditions $\dot{\gamma}_0 \approx 1\text{--}100 \text{ s}^{-1}$, they trigger nonlinear responses sufficiently strong as to differentiate among the investigated materials.

Scanning electron microscopy

Fats were imaged before and after being subjected to oscillatory shear deformations. Prior to sampling, sheared fats were subjected to 25 oscillatory cycles ($\gamma_0 = 50\%$) and then carefully removed from the rheometer plate with the parallel disk in the zero strain position. Fat pieces (for both unsheared and sheared samples) were then carefully removed with a spatula at intermediate locations between the edge and the center of the samples and then sectioned. We did so, to avoid collecting overly fractured samples (e.g., at the edge of the parallel plates where shear rates tend to be higher) or insufficiently deformed samples (e.g., at the center of the parallel plates where shear rates tend to be lower) and to minimize sample damage. To visualize the microstructural features of the fat crystal network is necessary to remove the liquid oil using solvents, which have shown to retain the structural integrity of the solid crystalline network to great extent (Chawla et al. 1990; Heertje 1993). This was achieved by suspending thin sample pieces in a ratio of 1:25 fat solvent. Ductile fats (D1 and D2) were suspended in a 8:2 (v/v) isobutyl alcohol-hexane mixture to enhance removal of the more-confined oil phase, while brittle fats (B1 and B2) were suspended uniquely in isobutyl alcohol (Chawla et al. 1990). Shortenings were statically deoiled at 20 °C (roll-in fat) and 14 °C (brittle fats) for 48 h, filtered (Whatman No. 5) to remove solvent and liquid oil, and finally allowed to stand on filter paper overnight to vaporize any remaining solvent. Minor structural changes include smoothing of the edges of crystal aggregates due to partial dissolving of triacylglycerols in the solvent during deoiling (Heertje 1993). Cryo-SEM was used to image the microstructure of the samples. The samples were then attached to the copper sample holder using the Tissue-Tek embedding medium. The sample holder was immersed in a liquid nitrogen slush (-207 °C) using an Emitech K1250x Cryo-preparation unit (Ashford Kent, UK), freeze-fractured to expose internal planes of the microstructure, and sputter-coated for 2 min with gold using a 20 mA deposition current, 7 nm min⁻¹ deposition rate. The sample holder was transferred to the SEM stage (Hitachi S-570, Tokyo, Japan) with accelerating voltage of the electron beam of 10 kV. Images were captured digitally using the Quartz PCI imaging package (Quartz Imaging Corp., Vancouver, Canada).

Ultra-small angle X-ray scattering

Data collection and data analysis

Samples were prepared in the form of fat disks with approximate dimensions of 20 mm × 1 mm (diameter × thickness) and were not subjected to oscillatory shear. Samples were then mounted into Grace Bio-Labs (OR, USA) circular silicon

isolators, and the isolator sides were sealed with microscope covers to contain the sample.

The 1D collimated mode (Long et al. 1991) using the Bonse Hart Instrument (Ilavsky and Jemian 2009; Ilavsky et al. 2012) at Argonne Photon Source (APS, Argonne National Laboratory) sector 9 was used for the X-ray scattering experiments. This instrument makes use of two sets of crystals pairs: the collimating set and the analyzer set. The USAXS geometry utilizes multiple crystal reflections to provide ultra-high resolution only in the vertical direction. By rotating the analyzer crystal pair using small steps, the scattered intensity at various angles can be measured with an extremely high angular precision or resolution. A complete operational description of the instrument can be found elsewhere (Ilavsky et al. 2013). Data collected was numerically desmeared to recover the differential scattering cross section (Lake 1967). Instrument control and data acquisition were performed using the Spec software for diffraction experiments. Each data point is one measurement for either 0.5, 1, or 2 s, as one goes from lower to higher q (Å⁻¹). *Indra* and IgorPro-based software were used for data reduction, removal of multiple scattering, and to determine the absolute intensity. The *Irena* (Ilavsky and Jemian 2009) IgorPro-based software was used for data interpretation using the unified fit (Beaucage 1995, 1996) and the Guinier-Porod model (Hammouda 2010). Both models, implemented in the *Irena* software, employ a nonlinear regression analysis to find the best-fitting parameters. Two repetitions for each sample were analyzed, and the average of the fitting parameters given by unified fit and Guinier-Porod models was reported.

USAXS data analysis

During USAXS, the scattering intensity is measured as a function of the scattering vector q , defined as $q = \frac{4\pi}{\lambda} \sin\left(\frac{4\pi}{\lambda}\right)$ where θ is the scattering angle and λ the wavelength of the incident X-ray. An estimation of the length scale (L) of the material probed can be obtained from the relation $L = 2\pi/q$. It is relevant to note that the Bonse-Hart system permits the collection of a sufficient number of data points in only a few minutes to cover the range ~ 100 nm $< L < 10$ –30 μ m. The scattering patterns were analyzed to find $I(q)$ vs. q regions that either follow Guinier scattering or Porod-power law scattering.

Equation 5 shows the unified fit model expression (Beaucage 1995, 1996).

$$I(q) = Ge^{-\left(\frac{q^2 R_g^2}{3}\right)} + \frac{B}{q^P} e^{-\left(\frac{q^2 R_g^2}{3}\right)} \left[\text{erf}\left(\frac{-qR_g}{6^{1/2}}\right) \right]^{3P} \quad (7)$$

where P is the Porod exponent that yields information on the structure of the aggregate and R_g is the radius of gyration. The exponential term $e^{-\left(\frac{q^2 R_g^2}{3}\right)}$ shows that the unified fit model represents all scattering objects as approximately spheres,

where i represents the structural level under study, while $i - 1$ indicates the previous level. The first term in Eq. 7 describes the Guinier region, valid for $q \leq q_1$, and the second term, the Porod power law valid for $q \geq q_1$. The requirement is that the Guinier and Porod terms, together with their derivatives, must be continuous at q_1 . G and B are the Guinier and Porod scale factors, respectively, with G related to the volume of the scatterers and B containing specific scattered surface area information.

We focus on the R_g and P parameters that come out of fitting the data to the unified fit model. The systems were discovered to be fractal in nature as observed by a straight line in the q region observed in two or three sections. It is noteworthy that the radius of gyration R_{g3} in the third region was held constant to fit the power law slope P_3 and hence was not used to draw conclusions pertaining the size of the scatterers.

When a fractal interpretation is given to the data, the P value gives information about the fractal dimension of the scatterers. A value of $|P| = 4$ indicates a scatterer or particle with a smooth surface and a fractal dimension $D_s = 2$. If $3 \leq |P| < 4$ then $6 - |P|$ is the surface fractal dimension ($2 < D_s \leq 3$). When $1 \leq |P| < 3$, then the value of $|P|$ is the fractal dimension, $D = |P|$. But if $|P| > 4$, all that is known is that there is diffuse interface (Beaucage 1995, 1996).

The other model used for interpretation of the scattering data was Guinier-Porod. This model, a variation of Eq. 7 (Hammouda 2010), considers that the primary particles can have shapes other than spherical, indicated by the terms involving s_1 and s_2 in Eq. (8). The value of the parameter s indicates platelets when $s = 2$, cylinders or rods when $s = 1$, and spheres when $s = 0$. Similar to the unified fit model, parameters like the radii of gyration and the power law exponents are obtained. The difference is that this model defines a structural level in a wider q region, in that each structural level can have multiple radii of gyration and power law slopes—as long as the scattering comes from one population of primary particles. The fitting functions are

$$\begin{aligned} I(q) &= \frac{G_2}{q^{s_2}} e^{\left(\frac{-q^2 R_{g2}^2}{3-s_2}\right)} & q \leq q_2 \\ I(q) &= \frac{G_1}{q^{s_1}} e^{\left(\frac{-q^2 R_{g1}^2}{3-s_1}\right)} & q_2 \leq q \leq q_1 \\ I(q) &= \frac{B}{q^P} & q \geq q_1 \end{aligned} \quad (8)$$

where the limits q_1 and q_2 are chosen manually by the experimentalist.

Results and discussion

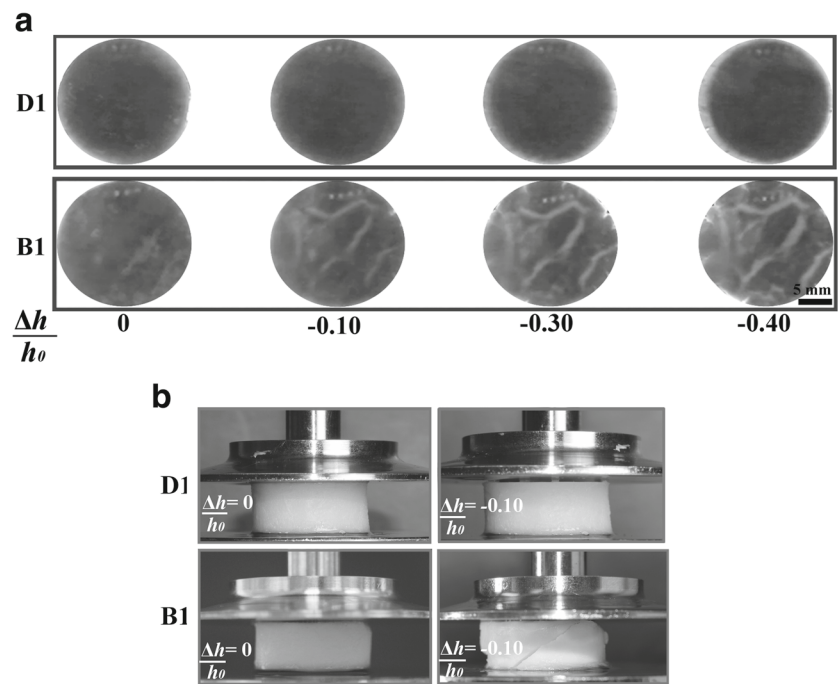
Figure 1 depicts macrographs of two fat samples lending evidence of ductile D1 and brittle B1 material deformation

during the application of axial normal force. Similar behaviors were observed for ductile D2 and brittle B2 (see supplementary material Fig. A8). Views from below (Fig. 1a) demonstrated that the surface of D1 remained mostly crack free within the middle of the parallel plate (DIA = 20 mm), unlike B1 where the formation of a number of large cracks was evident throughout the samples. Views from the side (Fig. 1b) and stress-strain curves (Fig. 2) also revealed that D1 specimens underwent larger plastic deformation, when compressed up to $\epsilon_c = 0.15$, whereas B1 test pieces could not sustain the applied compressive strain, showing a nonmonotonic behavior in the strain-stress curve (local maximum), and cracked more readily, displaying a cleavage line. The hysteresis in the stress-strain curves (Fig. 2) suggests that D1 absorbed more energy due to extensive plastic flow compared to B1, which are hallmarks of ductile and brittle solids, respectively. These observations are in agreement with van den Tempel (1958) who suggested that in hard brittle fats, shear trigger cracks which are not visible in liquid-like soft fats, but nevertheless did not provide experimental visual evidence of such cracks. In the following sections, we provide further evidence for drawing a parallel between the failure of fats under shear and the fracture of ductile and brittle solids.

Effect of sample thickness on rheological material functions

During shear rheology, it is assumed that materials deform homogeneously throughout the gap and remain in continuous contact with the plate periphery (Ewoldt et al. 2015). However, nonuniform flow phenomena such as wall slip and shear banding are particularly prevalent in pasty materials, particularly when using parallel plate configurations for rheological characterization (Ewoldt et al. 2015). To ensure that the measured material functions reflect the true behavior of the investigated materials, the effect of sample thickness Th (and thus gap height) on the average or first harmonic viscoelastic moduli G'_1 and G''_1 was determined. The viscoelastic moduli G'_1 and G''_1 are the most commonly used descriptors to quantify SAOS and LAOS responses, and they refer to the same generic notation G' and G'' as output by the rheometer. Figure 3a–c illustrates stress perspectives of strain-sweep tests with their respective plots of strain (γ_0) versus the stress of the first harmonic (τ_1) which contrast between the behavior of ductile-like and brittle-like fat materials. For D1, G'_1 and G''_1 nearly overlap for $Th = 1.3, 1.5$ mm, while for B1, G'_1 and G''_1 superimpose for all sample thickness except at $Th = 2$ mm (Fig. 3a, b). The lack of overlap at different thickness is an indication of slip, internal fracture planes, or other nonideal kinematics that deviate from homogeneous simple shear. It is observed for D1 that as sample thickness increases, the peak stress and its associated strain decrease dramatically caused

Fig. 1 Macroscopic evidence of ductile (D1) versus brittle (B1) deformation of representative fats during compression. **a** Views from below a transparent bottom plate for specimens with diameter = 20 mm and thickness $Th = 2$ mm. **b** Side views for specimens with thickness $Th = 10$ mm. A ductile fat (D1) plastically deforms, whereas a brittle fat (B1) fails showing cracks and a cleavage line at $\Delta h/h_0 = -0.10$. At higher deformations, ductile (D1) also shows cracks that onset at the periphery of the test piece triggered by shear stresses



possibly due to interplay between slip and shear banding (Thomas 1961) preceding failure (Fig. 3c). In contrast, it is observed for B1 that at $h = 2000 \mu\text{m}$, the peak strain (but not the magnitude of the stress) shifted to lower strain amplitudes arguably due to wall slip. These trends, albeit not rare to the rheometry of pastes, resonate with the behavior of brittle solids and ductile solids in which slip and shear strain localization are recurrent (Thomas 1967). Nevertheless, we caution the reader that identifying the true cause of this behavior is not trivial as other factors such as structural changes or additional flow instabilities might also be at play (Divoux et al. 2015).

Linear to nonlinear viscoelasticity

Based on the aforementioned experiments, we used a thickness = 1.3 mm for further rheological experiments as the

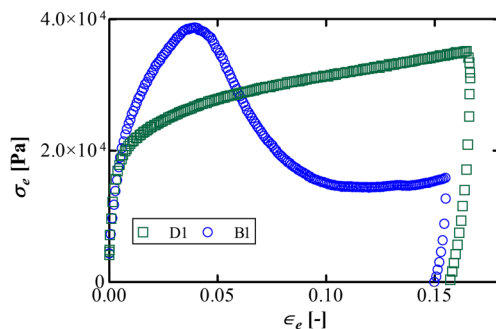


Fig. 2 Compressive engineering stress ($\sigma_e = F/A_0$) as a function of compressive engineering strain ($\epsilon_e = \Delta h/h_0$) for a representative ductile (D1) and brittle (B1) fat. The dimensions of the specimens were $20 \text{ mm} \times 10 \text{ mm}$ (DIA \times height). A thin layer of mineral oil was applied to the parallel plate geometries to diminish Frictional force at the edges

impact of shear instabilities was less prominent. At $Th = 1.3 \text{ mm}$, it was observed that the linear viscoelastic moduli G'_1 and G''_1 and the yield stress τ_{yield} , determined as the maximum stress (which is mainly elastic), remained unremarkable, e.g., D1 and D2 have storage moduli nearly two times smaller than B1 but similar to B2, and yield stress smaller than B1 by $\sim 400\text{--}800 \text{ Pa}$ and larger than B2 by $\sim 1000 \text{ Pa}$ (Table 1). This is agreement with our previous study in which we found that triglyceride shortenings may share similar linear elastic moduli and yield stress irrespective of their bulk functionality (Macias-Rodriguez and Marangoni 2016a). Pertaining to the nonlinear LAOS behavior, G'_1 and G''_1 decreased indicating that elastic softening and viscous thinning of the crystal network (e.g., disturbance of network interactions) dominate the average stress response. Moreover, when plotted as a function of input strain amplitude (see supplementary material Fig. A7), G'_1 also decreased continuously but G''_1 rose initially at $\gamma_0 \approx 0.09\%$, reached a local maximum at $\gamma_0 \approx 0.57\%$, and then dropped monotonically, crossing-over G'_1 at $\gamma_0 \approx 1\text{--}2\%$. The G''_1 maxima is typical of type III materials which exhibit a weak strain overshoot or “Payne effect” as termed in filled elastomers (Hyun et al. 2002). In fat crystal networks, the underlying reasons of G''_1 maxima and crossover of $G'_1 = G''_1$ are unknown. Previous studies have associated G''_1 weak overshoot to the onset of disruption of intercluster bonds, material fluidization, expulsion, and drainage of interstitial fluid within microstructure due to failure or compression of the gel network in other colloidal gels at moderate and high volume fractions (Laurati et al. 2011; Kim et al. 2014).

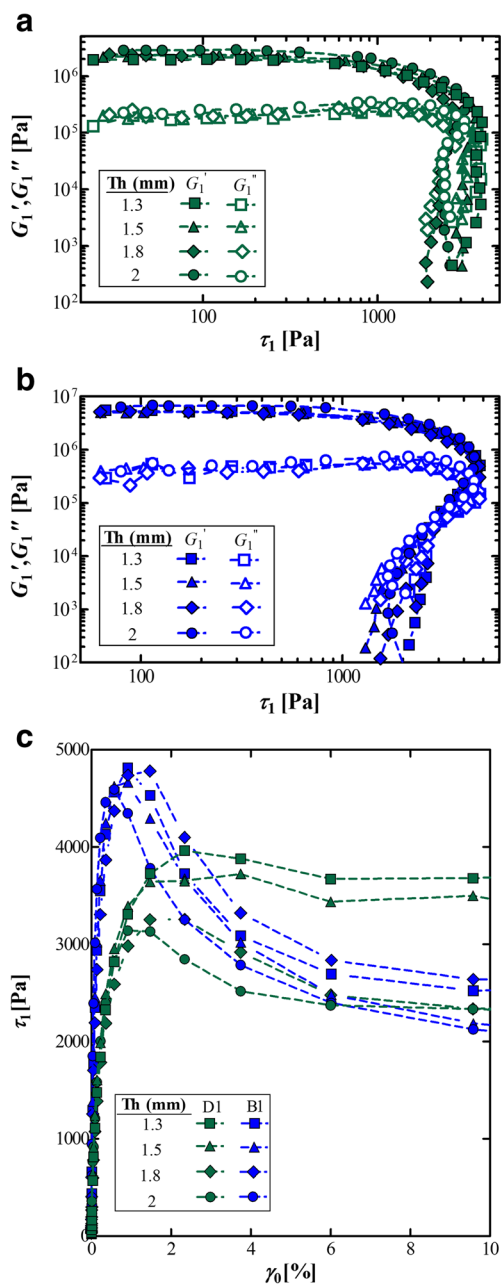


Fig. 3 **a, b** First harmonic viscoelastic moduli as a function of stress response for **a** ductile fat D1 and **b** brittle fat B1. **c** First harmonic stress amplitude τ_1 as a function of apparent strain amplitude γ_0 for both fats. Data was obtained from strain amplitude sweeps $\gamma_0 = 0.001$ –100%, $\omega = 3.6 \text{ rad s}^{-1}$ for increasing sample thickness $\text{Th} = 1.3$ –2 mm to detect shear instabilities. The strain range $\gamma_0 = 0.001$ –10% in **c** was chosen to emphasize differences in mechanical behavior; prominent slip was observed above $\gamma_0 = 10\%$. All data shown in subsequent figures fall within this range

At first glance from Fig. 3, the behavior of G'_1 and G''_1 beyond the linear region appeared comparable across the different material classes. Upon closer inspection, it can be noted that G'_1 and G''_1 for D1 and B1 showed strikingly different failure patterns. As can be seen, D1 G'_1 and G''_1 displayed a

steady decrease starting at $\tau_1 \approx 1000$ Pa. In contrast, B1 G'_1 and G''_1 showed an initial gradual decrease starting at $\tau_1 \approx 1500$ Pa followed by an abrupt drop and backward bending at $\tau_1 \approx 4000$ Pa, evoking sudden failure as the strain amplitude increases. These markedly different responses can be also visualized in the stress amplitude versus strain amplitude plots (Fig. 3a, 3b, $\text{Th} = 1300 \mu\text{m}$). Both samples remained in the elastic regime up to small critical strains $\gamma_0 \approx 0.05\%$, which is typical for materials such as fat crystal networks interacting via short-range interparticle forces (van den Tempel 1961). It also appeared that D1 displayed more plastic deformation than B1. Both samples reached peak maxima of $\tau_1 \approx 4000$ Pa and $\tau_1 \approx 4900$ for D1 and B1, respectively. Beyond the peak maxima, the stress in D1 roughly plateaus as compared to B1 in which the stress suddenly drops (similar to the compression test in Fig. 2). Similar findings are reported for D2 and B2 (see supplementary material Fig. A8). These mechanical signatures are similar to those observed for ductile and brittle solids. While ductile solids exhibit significant plastic straining upon failure, brittle solids exhibit little, if any, inelastic deformation prior to catastrophic fracture (Thomas 1961). By analogy with solid materials, we thus propose that D1 and D2 act as ductile viscoelastic solids, manifested by larger plastic strains (visualized as the decrease of the local slope in the stress deformation curve) and a plateau effect, while B1 and B2 resemble brittle viscoelastic solids, evidenced by larger elastic straining and peak stress that dramatically decreases post-failure. These behaviors are in good agreement with our previous study (Macias-Rodriguez and Marangoni 2016a, b), in which the evolution of the third-order leading Fourier harmonic displayed similar qualitative behavior and are consistent with Fig. 2, suggesting that yielding of fat crystal networks under compression and oscillatory shear are the consequence of a similar underlying phenomenon.

To provide a physical picture of the mechanisms involved in yielding of ductile (D1, D2) and brittle (B1, B2) fats, we analyzed the LAOS stress signals using Lissajous-Bowditch curves, Chebyshev decomposition, and the local nonlinear elastic and viscous metrics proposed by Ewoldt et al. (2008). LAOS analysis was performed at a fixed frequency of $\omega = 3.6 \text{ rad s}^{-1}$ and strain range of $\gamma_0 = 0.01$ –10% to map deformation rates relevant to the industrial rolling process and probe sufficiently large deformations, nearly three orders of magnitude larger than linear deformations (Chakrabarti-Bell et al. 2010; Macias-Rodriguez and Marangoni 2016a). For illustrative purposes, third harmonic elastic and viscous Chebyshev coefficients are shown in Fig. 4 to denote departure from linearity. Elastic and viscous L-B curves for each material class (D1 and B1) are shown in Figs. 5 and 6. Lissajous-Bowditch curves for the remaining samples and 3D Lissajous-Bowditch curves for two representative samples are included in the supplementary material (Figs. A8–A11).

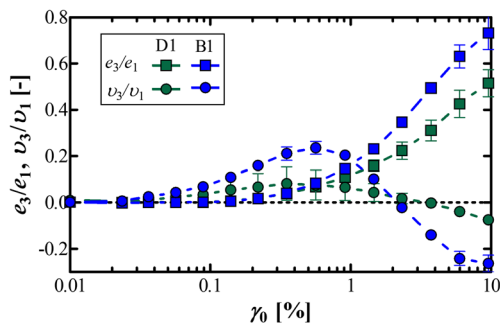


Fig. 4 Scaled third-order elastic e_3/e_1 and viscous v_3/v_1 Chebyshev coefficients as a function of strain input γ_0 at $\omega = 3.6 \text{ rad s}^{-1}$ for ductile D1 and brittle B1 fats

Corresponding elastic and viscous rheological fingerprints for all samples are presented in Figs. 7 and 8.

Chebyshev coefficients and Lissajous-Bowditch curves

Higher order Chebyshev coefficients indicate departure from the linear regime and augment the physical interpretation provided by G'_1 and G''_1 in the LAOS regime. Leading order Chebyshev coefficients e_3/e_1 and v_3/v_1 capture changes in the local elastic and local viscous stresses of the decomposed signal which manifest as the convexity (bending or twisting) in Lissajous-Bowditch curves (see Figs. 5 and 6). Most importantly, the signs of these third harmonics indicate the driving cause of the deviation from linearity in G'_1 and G''_1 (i.e., whether they are caused primarily by large strains or large strain rates) (Ewoldt and Bharadwaj 2013).

Within the linear regime $\gamma_0 \leq 0.03\%$, e_3/e_1 and v_3/v_1 did not contribute greatly to the stress response as expected. At $\gamma_0 \approx 0.05\%$, e_3/e_1 remained marginal, whereas v_3/v_1 began to

rise signaling the onset of nonlinearities and indicating that viscous shear thickening of G''_1 was driven by large strain rates (a viscoelastic fluid type of response), since $v_3/v_1 > 0$. At larger strain amplitudes, v_3/v_1 changes signs. In this regime, there is also a change from thickening to thinning of G''_1 (see Fig. A7). Based on the sign of v_3/v_1 , large rates also seem to drive this nonlinearity. One must be cautious of the sign interpretation beyond the leader order deviation. It requires the third harmonic to determine the curvature of the viscous stress, which is generally but not always the case for the L-B curves in Figs. 5 and 6. For the elastic measures, there is a decrease in G'_1 (see Fig. A4), and e_3/e_1 is initially positive, indicating that elastic softening was driven also by large instantaneous strain rates. Overall, similar behavior was observed for brittle and ductile fats; however, it appeared that B1 exhibits stronger nonlinearities represented by higher and lower magnitudes of elastic and viscous Chebyshev coefficients, respectively.

Lissajous-Bowditch curves were used to gain qualitative insight into the nonlinear viscoelasticity of ductile and brittle fats. Lissajous-Bowditch figures are parametric plots of strain versus stress (elastic perspective) or strain rate versus stress (viscous perspective) which appear elliptical in the linear region, and acquire complex shapes in the nonlinear region, due to the presence of higher harmonic components. Elastic and viscous L-B curves are depicted in Figs. 5 and 6 for ductile (D1) and brittle (B1), respectively. For both material classes, linear viscoelasticity dominated the stress response at strain amplitudes $\gamma_0 < 0.05\%$ (not shown), supported by tight elliptical L-B shapes. At strains $\gamma_0 \geq 0.09\%$, L-B began distort because of periodic variations in the stress response, especially visible at local minima and maxima, with a visibly noticeable onset of nonlinear viscoelasticity in accordance with the trends observed for v_3/v_1 and e_3/e_1 . At $\gamma_0 \geq 0.57\%$, D1 and B1

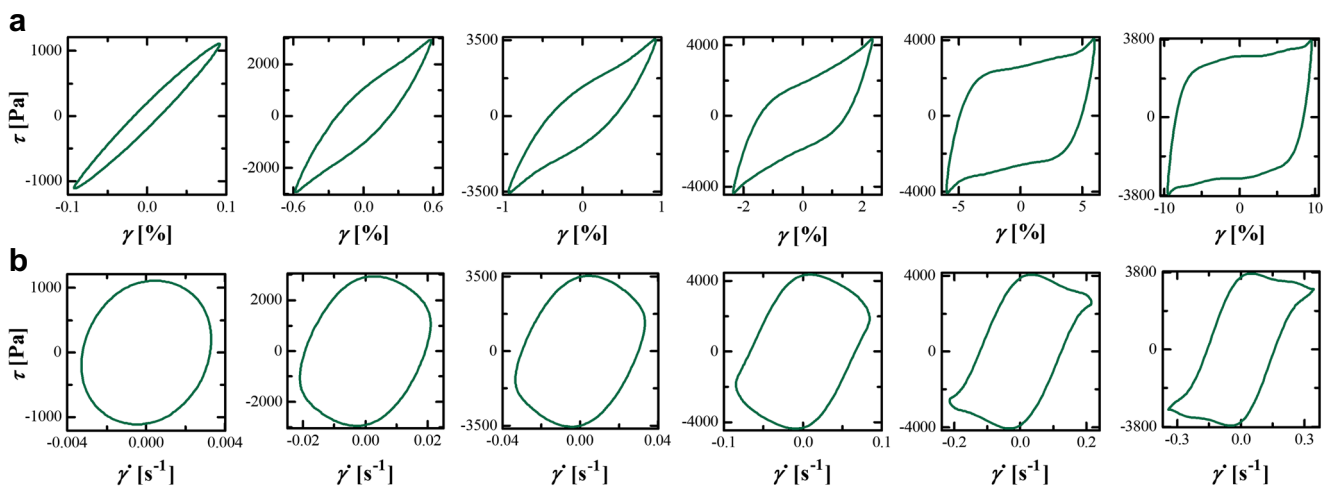


Fig. 5 Lissajous-Bowditch curves for a ductile (D1) fat at $\omega = 3.6 \text{ rad s}^{-1}$. **a** Individual plots of absolute stress τ vs. strain γ (elastic perspective). **b** Individual plots of absolute stress τ vs. strain rate (viscous perspective).

Plots were obtained for selected strain values within $\gamma_0 = 0.01\text{--}100\%$, after the application of 25 oscillatory cycles. Typically the last 3–5 cycles were employed for data analysis

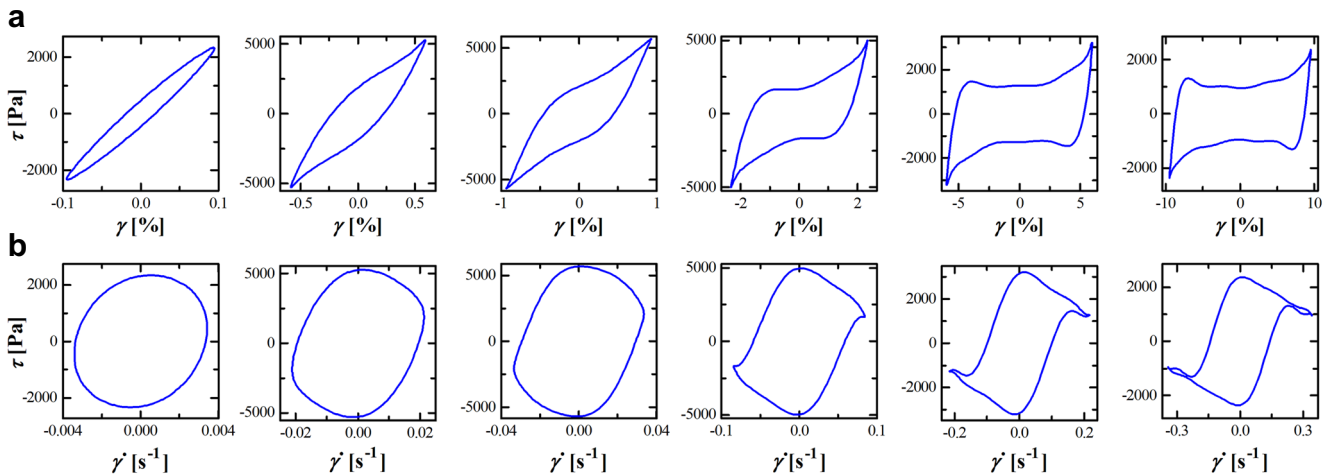


Fig. 6 Lissajous-Bowditch curves for a brittle (B1) fat at $\omega = 3.6 \text{ rad s}^{-1}$. **a** Individual plots of absolute stress τ vs. strain γ (elastic perspective). **b** Individual plots of absolute stress τ vs. strain rate (viscous perspective).

Plots were obtained for selected strain values within $\gamma_0 = 0.01\text{--}100\%$, after the application of 25 oscillatory cycles. Typically, the last 3–5 cycles were employed for data analysis

displayed qualitatively similar features, including stress upturns or “twists” in the elastic Lissajous-Bowditch curves at

the largest instantaneous strain γ_0 for each oscillatory cycle, indicating lower elastic energy storage at minimum strain γ_{\min} (which is the location of largest strain rate), compared to elasticity at maximum strain within a cycle. This was concurrent with the appearance of “bends” in the viscous curves also at $\dot{\gamma}_{\max}$ indicating pseudoplasticity or shear-thinning behavior, which was least prominent in D1. Eventually, the nonlinear response is strongly nonlinear at $\gamma_0 \geq 6\%$, as to induce self-intersections and secondary loops in the viscous Lissajous-Bowditch curves at $\dot{\gamma}_{\min}$, which are more apparent in B1. The appearance of secondary loops have been physically related to strong unloading of instantaneous elastic stresses (which occurs faster than accumulation of new elastic deformations) and competition between network destruction and formation at high shear rates (Ewoldt and McKinley 2010; Jacob et al. 2014). Quantitatively speaking, this translates to negative values on the instantaneous elasticity G'_M or values alternating from positive to negative if multiple loops are present. Qualitatively speaking, self-intersections correspond to strong overshoots ($\gamma_0 \geq 2.34\%$) during yielding which are particularly more pronounced in B1 (Fig. 3c). Within a LAOS cycle, e.g., elastic L-B curve at $\gamma_0 \approx 6\%$ (Fig. 6), this peak in stress demarks two regions: a nearly linear region preceding the overshoot that extends roughly from the lower reversal point to the stress overshoot (Fig. 6) and a “flow” region following the overshoot. This linear stress region has been associated with cage or residual elasticities by other researchers (Rogers et al. 2011; van der Vaart et al. 2013; Kim et al. 2014). In the flow region, as shear rate increases (or strain decreases), the stress decreases reaching a minimum. Subsequently, as the strain increases (or shear rate decreases), the stress increases again indicating thixotropy or network restructuring as previously observed (Macias-Rodriguez and Marangoni 2016a). This progresses until the end of the half-cycle (γ_{\max} and $\dot{\gamma}_{\min}$), and then, the sequence is repeated

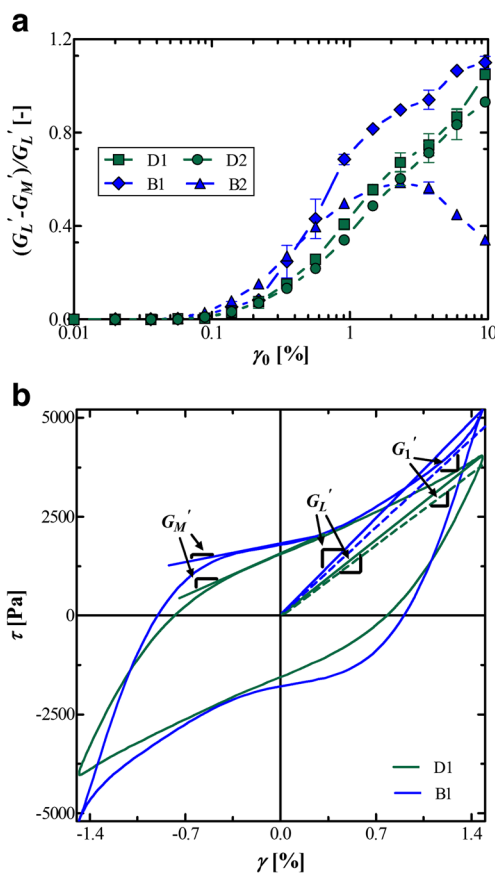


Fig. 7 **a** Normalized difference between local elastic measures: minimum strain (G'_M) and large strain modulus (G'_L) as a function of strain input γ_0 at $\omega = 3.6 \text{ rad s}^{-1}$ for ductile (D1, D2) and brittle fats (B1, B2). **b** Lissajous-Bowditch curve (elastic perspective) showing strain γ_0 versus stress τ for a selected data point $\gamma_0 = 1.47\%$, displaying graphical representation of local (instantaneous) and global (average) LAOS elastic measures

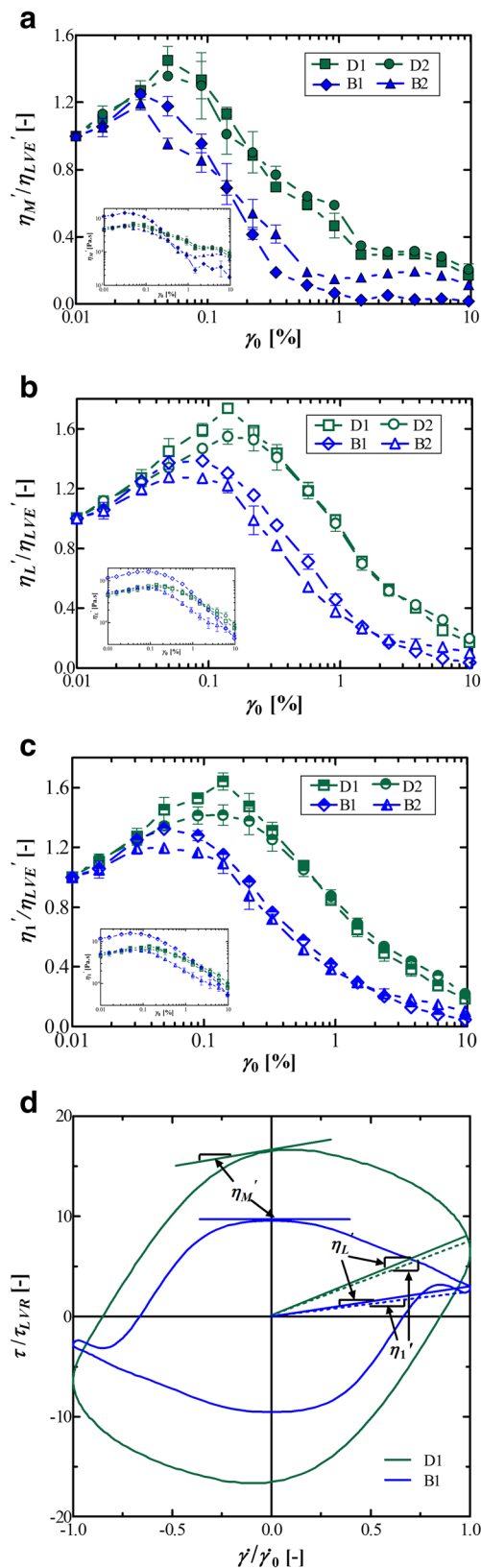


Fig. 8 Dynamic viscosities as a function of strain input γ_0 at $\omega = 3.6 \text{ rad s}^{-1}$ for ductile (D1, D2) and brittle (B1, B2) fats. **a** Minimum strain rate η_M' . **b** Large strain rate η_L' . **c** Average strain rate viscosities η_A' . Insets show viscosity metrics normalized by η_{LVE}' at $\gamma_0 = 0.01\%$. **d** Lissajous-Bowditch curve (viscous perspective) showing normalized shear rate $\dot{\gamma}/\dot{\gamma}_0$ versus stress τ normalized by τ_{LVE} at $\gamma_0 = 0.01\%$, for a selected data point $\gamma_0 = 1.47\%$ ($\dot{\gamma}_0 = 0.05 \text{ s}^{-1}$), displaying graphical representation of local (instantaneous) and global (average) LAOS viscosity measures

more evident in D1. Similar intracycle LAOS responses were recently reported by Ramamirtham et al. (2017) in tribehenin dispersed in isopropyl myristate and other yielding colloidal systems (Kim et al. 2014). Ramamirtham et al. (2017) attributed such nonlinearities to the shape of the crystal aggregates: bundles of needle aggregates displayed greater viscous-like behavior and complete fluidization, while spherical aggregates showed greater plastic-like behavior. Such behavior is somewhat similar to the brittle-like behavior and ductile-like behavior reported here, respectively, though we did not observe full material flow as we employed relatively small strain amplitudes (due to the shear instabilities observed here) compared to Ramamirtham et al. (2017) (up to $\gamma_0 = 1000\%$). Kim et al. (2014) measured the time-dependent moduli R' and R'' in dense heterogeneous colloidal gels, and identified a series of nonlinear events which included elastic straining, elastoplastic softening, and viscoplastic behavior (all in the nearly linear region), followed by yielding and flow. After shear flow reversal, only flow and restructuring occurred. In our study, secondary peaks or oscillations were observed which follow the primary yielding peak. Although, these peaks manifested in a variety of colloidal systems (i.e., soft star-like micelles, nanoemulsion gels), in our case, these features seem to be artifacts resulting mainly from data processing (e.g., see Fig. A5 where consideration of higher order harmonics led to better waveform reconstruction).

Nonlinear viscoelastic metrics

As alluded to earlier, typical mechanical characteristics of ductile solids include greater ability to retain strength during yielding in concert with larger viscous dissipation and plastic deformation than brittle solids. To capture these behaviors, we adopt local (or instantaneous) nonlinear descriptors as proposed by Ewoldt et al. (2008), a selection of which are displayed in Figs. 7 and 8, along with their corresponding graphical representation. To ease comparisons between ductile and brittle fats, measures were also normalized to their linear properties (η_{LVE}') when applicable. These local measures complement average measures as shown in Fig. A7 (see supplementary material), which denote global elastic strain softening and global viscous thickening and thinning, both driven by large strain rates as previously elucidated. As described earlier, after failure ($\gamma_0 \approx 2\%$) the strain-stress response is apparent. However, the total energy dissipated and energy

during flow reversal. Moreover, larger areas are enclosed by the elastic Lissajous-Bowditch curves at sufficiently high strains ($\gamma_0 \geq 6\%$), indicative of plastic deformation which is

stored are true, as measured with loads and displacements at the boundary, which allows for meaningful comparison of material functions between ductile and brittle fats. Nonlinear elastic properties are presented as relative differences between the large strain or secant modulus G'_L and the minimum strain or tangent modulus G'_M , which indicate more elasticity at the turnaround point G'_L than during flow G'_M . This leads to stress upturns within a cycle (or local strain stiffening as referred in the literature), as observed in the elastic L-B curves. It is shown that the general qualitative elastic behavior of ductile and brittle fats was similar, except for B2, which plateaued earlier and then decreased given its much lower yield stress τ_y . It is noteworthy to mention that the magnitudes of G'_M and G'_L give an underestimation of intracycle elasticity as they suffer from plastic strain accumulation since they are calculated post-yielding (Dimitriou et al. 2013). Nevertheless, based on the qualitative insight gained from L-B curves and the fact that fats do not display marked high elasticity, we conclude that elastic properties do not dominate the nonlinear response. By contrast, viscous measures showed striking differences, e.g., dynamic viscosities at instantaneous minimum strain rates η'_M and large strain rates η'_L denoted less apparent thinning for ductile D1 and D2 compared to brittle B1 and B2 fats. For instance, in nearly two decades of deformation ($\gamma_0 = 0.01$ – 0.92%), η'_M/η'_{LVE} and η'_L/η'_{LVE} decreased 41–53 and ≤ 5 –8% for D1 and D2, compared to 85–93 and 54–62% for B1 and B2. In agreement with the viscous Chebyshev coefficients v_3/v_1 , it is observed that the average dissipated energy η'_1 is driven mainly by intracycle viscous dissipation occurring at large instantaneous strain rates η'_L . The increased energy dissipation of D1 and D2 compared to B1 and B2 resonates with the ductile-like behavior and brittle-like behavior of the samples, respectively, in analogy with solid materials. Here, using LAOS stress decomposition, we can isolate that nonlinear viscous effects change, but nonlinear elastic effects do not, across these material classes. It has been suggested that during deformation, a ductile solid converts the vast majority of the released strain energy into other types of energy, mainly dissipative, associated with plastic flow, whereas a brittle solid expends a large amount of energy for crack growth or formation of new surfaces (Irwin 1948; Orowan 1949).

Structural characterization

As earlier mentioned, fat crystal networks feature structural hierarchies from molecular to microscopic dimensions. These multiple length scales determine the rheological behavior of these materials (Marangoni et al. 2012). In this paper, we investigated “quiescent” structural length scales (L) ranging from ~ 20 nm to $6 \mu\text{m}$ using USAXS and SEM techniques, as we had described the molecular length scale of the samples in

a previous study (Macias-Rodriguez and Marangoni 2016b). Figure 9 shows absolute intensity $I(q)$ as a function of scattering vector q obtained from USAXS experiments. In general, the USAXS patterns yield “hints” about the investigated structures: the linear (power law) and Porod regions of the log-log plots convey information about the distribution of different length scales (i.e., each line represents a structural level conforming to a fractal character) and average sizes of the scatterers, respectively (Peyronel et al. 2014a). As shown in Fig. 9, ductile fats D1 and D2 exhibit three-hierarchy structures, whereas brittle fats B1 and B2 display two-hierarchy structures (Peyronel et al. 2014a). To characterize these data, we relied on the unified fit model and Guinier-Porod model (Beaucage 1995, 1996; Hammouda 2010), with their best-fitting parameters shown in Table 2, and previous USAXS experiments and computer simulations performed in complex fat systems at intermediate volume fraction (Quinn et al. 2014; Peyronel et al. 2014b; Pink et al. 2015). These parameters and their interpretations collectively describe the aggregation mechanisms driving the formation of the crystal network, size, geometry, and structural features of the fundamental scatterers (crystal nanoplatelets (CNPs)) and crystal aggregates. Using the unified fit model, up to three structural levels or hierarchies were successfully fitted: level 1 and level 3, corresponding to high and low q ranges and level 2 referring to intermediate q values. The slope P_1 indicated that the first structural level was made up by CNPs with smooth ($P \approx 4$) interfaces in ductile fats and rough interfaces ($P < 4$) in brittle fats. Estimation of “particle” sizes given by the radius of gyration R_{g1} indicated that the primary scatterers of ductile fats were up to 11 times as small as those of brittle fats. The slope P_2 suggested that crystal platelets in ductile fats self-assembled into intermediate hierarchies obeying an interplay between solid condensation and solid diffusion ($P_2 > 2.1$) or DLCA mechanisms ($P_2 \approx 1.8$), as explained by previous models and computer simulations (Peyronel et al. 2014b; Pink et al. 2015). The crystal clusters had average sizes $R_{g2} = 490.2$ – 358.0 nm. The slope P_3 ($P_3 > 4$) suggested that in most of the cases, crystal clusters aggregated having diffuse interfaces (Beaucage

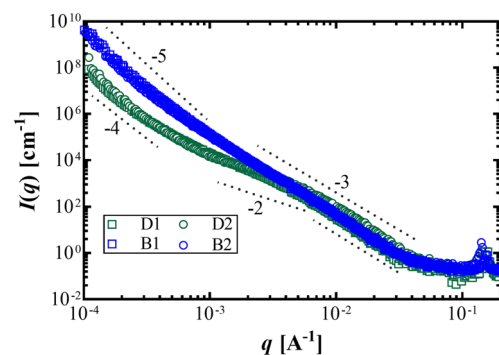


Fig. 9 Absolute scattering intensity $I(q)$ as a function of the scattering vector q . Slope values included in the plot serve as guides for the actual values obtained by the unified fit model and summarized in Table 2

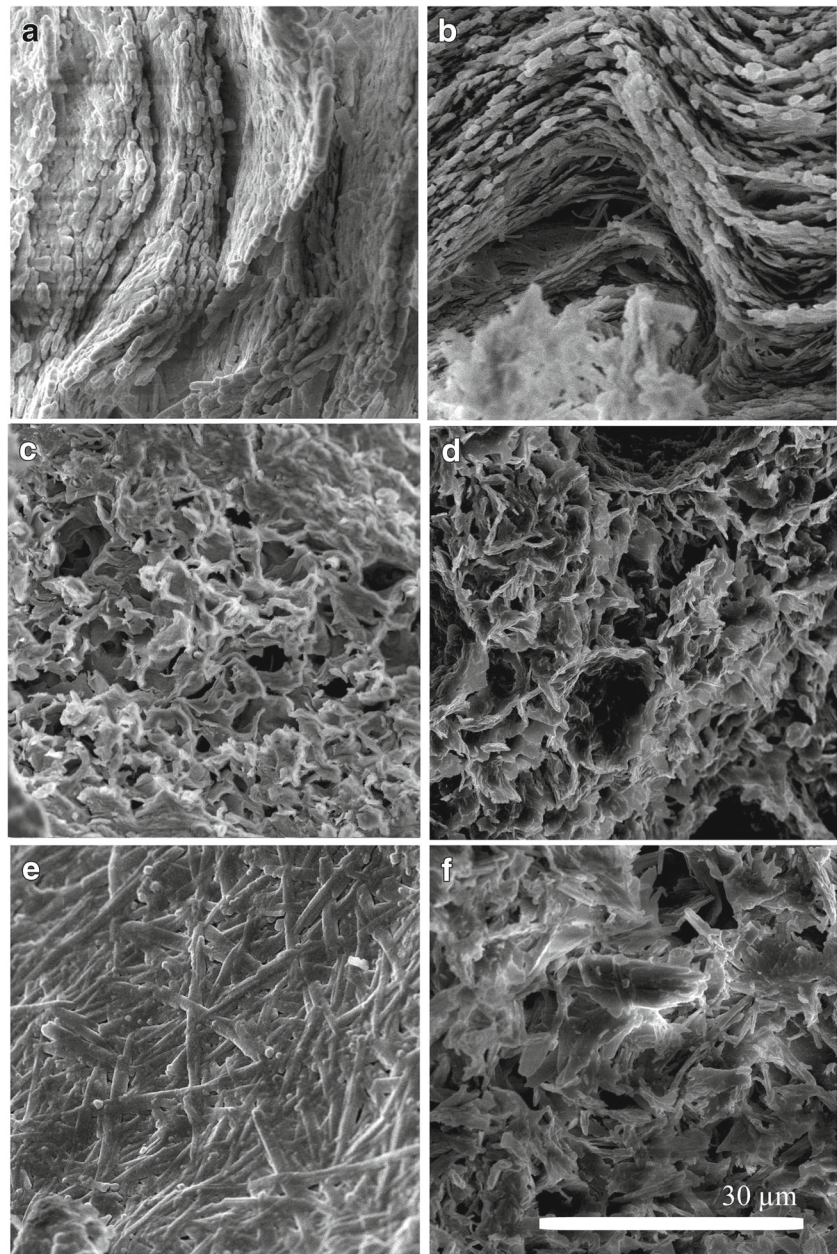
Table 2 Selected parameters obtained from unified fit and Guinier-Porod models and length scales probed in each structure level of the unified fit model. Standard error means for P and S parameters were equal or below 0.1

Sample	P_1	R_{g1} (nm)	L_1 (nm)	P_2	R_{g2} (nm)	L_2 (nm)	P_3	L_3 (μm)	S
D1	3.8	53.3 ± 2.4	21–157	2.3	490.2 ± 24.7	157–1571	3.7	0.6–6.3	1.7
D2	4.0	35.8 ± 0.7	13–78	1.7	358.9 ± 10.7	78–698	4.2	0.1–6.3	1.5
B1	3.5	399.8 ± 6.6	21–785	–	–	–	4.7	1.3–6.3	2.0
B2	3.5	167.4 ± 0.0	21–628	–	–	–	4.1	1–6.3	2.0

1996). Results from the Guinier-Porod model provided insight on the geometry of the scatterers resulting from CNP aggregation. It is suggested that either CNPs assembled at the mesoscopic scale into “supra-platelets” ($S=2$) or structures

with shapes intermediate between rods and platelets ($1 < S < 2$) (Hammouda 2010). To further visualize the microlength scales, SEM experiments were performed on nonsheared samples and samples after applying substantial nonlinear

Fig. 10 Cryo-scanning electron images of ductile (D1, D2) and brittle (B1, B2) fats. **a** D1. **b** D2. **c** B1. **d** B2. **e** D1 after deformation $\gamma_0 = 50\%$. **f** B1 after deformation $\gamma_0 = 50\%$. All images share the same magnification bar = $30 \mu\text{m}$



oscillatory shear deformations ($\gamma_0 = 50\%$). Overall, microstructural features shared similarities depending on whether the fat crystal network was ductile or brittle in nature. Figure 10 illustrates SEM micrographs obtained for the presented examples of ductile (D1, D2) and brittle (B1, B2) materials (refer to supplementary material Fig. A12 for similar micrographs at lower and higher magnifications). In general, the microstructure of D1 (Fig. 9a, b) appeared more homogeneous, composed of well-defined platelet-like crystal aggregates with variable size ($\sim 2\text{--}10\ \mu\text{m}$ length) interconnected into elongated layers, roughly parallel to each other, leaving interstitial channels in between, where the liquid oil might have been confined. It is speculated that the three-hierarchy level structure observed in USAXS enables the creation of such ordered long-layered structures at the micron length scale observed in ductile fats (D1 and D2). By contrast, brittle fats, B1 and B2 (Fig. 9c, d), comprised heterogeneous networks made of distorted or “flaky” sheet-like crystal aggregates of comparable size and microholes or voids ($\sim 16\ \mu\text{m}$ diameter) where presumably most of the liquid oil is entrained. The present microstructures are consistent with their processing regimes as substantial cooling and shearing typically result in an uniform, oriented microstructural network such those observed in D1 and D2 but not in B1 and B2 (Maleky et al. 2011). Upon substantial nonlinear deformations, it seemed that shear broke the continuity of the layered microstructure of D1 (Fig. 9e), and caused the nearly parallel array of crystallites to “squeeze” and induced their aggregation into twisting “fiber-like” aggregates with average lengths of $\sim 12\ \mu\text{m}$. These twisted aggregates lend qualitative evidence of ductile deformation. Lin-Gibson et al. (2004) suggested a somewhat analogous response for networks made up of softer elastic domains (nanotubes) suspended in a less viscous fluid which showed flow-induced clustering and vorticity-aligned elongation. In contrast, the aggregates making up the crystal network of B1 (Fig. 9f) fragmented, leading to a more random microstructure with element lengths of $\sim 7\ \mu\text{m}$. Kloek et al. (2005) estimated in fat dispersions of fully hydrogenated palm oil in sunflower oil defect sizes from which cracks nucleate (such as in brittle fats during compression, see Fig. 1) in the order of $10\ \mu\text{m}$ which corresponds to the length scale of the crystal aggregates observed by SEM in our study.

Linking rheology and structure and considering that the primary mechanical difference is with the *viscous* nonlinearities (rather than elastic nonlinearities, as revealed by LAOS), our interpretation is that elastic energies are stored within the hierarchical network in similar ways, but dissipation across the structural levels and crystallite layers is the key difference.

It can be speculated that in ductile fats, shear loads are better dissipated among the three-hierarchy structures unlike brittle fats where energy is exchanged only between two hierarchy levels. It can also be hypothesized that the microstructure provides mechanisms of alleviating or constraining local

stresses either by allowing controlled sliding motion of the elongated crystallite layers with the liquid phase acting like a lubricant in ductile fats or restricting motion of the “disordered” crystal aggregates in brittle fats. Overall, this provides a tentative explanation for the observed LAOS behavior and the formation of macroscopic cracks in brittle fats. Such a picture, it is not unreasonable as it has been demonstrated (via computer simulations) at a fundamental level that material toughness (“ductility”) and defect tolerance may vastly increase solely by introducing *as little as one* “extra” hierarchical structure in biological-like materials with similar constituents and volume fraction (Sen and Buehler 2011). Additionally, enhanced plasticity and toughening mechanisms in biological materials originates not only from the presence of multiple length scales but also from the incorporation of structural means, namely mineral-platelet sliding in seashells, for relieving locally high stresses (Ritchie 2011).

Conclusions

In previous studies, linear viscoelasticity has been the common explored territory in relating mechanical behavior to macroscopic performance and sensory attributes of fats. However, linking nonlinear viscoelasticity to macroscopic performance may be equally or far more relevant as most processing conditions and application uses of fats typically impose substantial nonlinear deformations. It is possible that fats with comparable linear viscoelastic properties diverge on their nonlinear behavior as supported by our results. Using the LAOS strain protocol, it was possible to quantitatively discriminate between ductile (roll-in) and brittle (all-purpose) fats. LAOS allows for decoupling energy storage and loss mechanisms in nonlinear rheology. A limitation of investigating the LAOS response of materials displaying time-dependent nonlinearities is that they might experience structural changes during measurement and hence affect the yielding response. A possible solution for this is to investigate the material at frequency and strain amplitude so that the system does not evolve over time. Given the long relaxation time-scales of fats, this was not possible. Using the present protocol, there were no important differences in the moduli of elasticity. Instead, the primary difference was the moduli of viscous dissipation; ductile fats were substantially more dissipative than brittle fats, in accordance with higher resistance to flow and plastic deformation for the ductile systems. These findings are in good agreement with the macroscopic behavior of the systems and their mechanical behavior under compressive stress. Structural investigations indicated that ductile fats featured an additional hierarchy level, and crystal aggregates ordered in elongated crystal layers unlike brittle fats that showcased only two hierarchy structures and more “disordered” crystal network. It is suggested that the hierarchy levels

and spatial distribution of the microstructure play a pivotal role on high energy *dissipation* (rather than energy storage) and hence superior load-bearing ability of ductile fats to endure mechanically demanding processes such as “cold-working.” These results call for further exploration of the relationship between rheology and structure under LAOS shear flow using space- and time-resolved techniques, and computer simulations to gain mechanistic insight of the yielding behavior of these soft materials.

Acknowledgements The authors are indebted to Dr. Jan Ilavsky and his team at beam line 9ID for their invaluable support and help through the data collection and analysis of USAXS. This research used resources of the Advanced Photon Source, a US Department of Energy (DOE) Office of Science User Facility operated for the DOE Office of Science by Argonne National Laboratory under Contract No. DE-AC02-06CH11357. We also greatly acknowledge Dr. Fernanda Peyronel (Food Science, University of Guelph) for helping with USAXS data reduction and interpretation, Dr. David Pink (Physics, St. Francis Xavier University) for discussions on USAXS, Mr. Gaurav Chaudhary for discussions on LAOS rheology (Mechanical Science and Engineering, University of Illinois at Urbana-Champaign), and Dr. Peter X. Chen (Food Science, University of Guelph) for helping with video recording.

References

- Acevedo NC, Marangoni AG (2013) Functionalization of non-interesterified mixtures of fully hydrogenated fats using shear processing. *Food Bioprocess Technol*:575–587
- Beaucage G (1995) Approximations leading to a unified exponential/power-law approach to small-angle scattering. *J Appl Crystallogr* 28(6):717–728. <https://doi.org/10.1107/S0021889895005292>
- Beaucage G (1996) Small-angle scattering from polymeric mass fractals of arbitrary mass-fractal dimension. *J Appl Crystallogr* 29(2):134–146. <https://doi.org/10.1107/S0021889895011605>
- Chakrabarti-Bell S, Bergström JS, Lindskog E, Sridhar T (2010) Computational modeling of dough sheeting and physical interpretation of the non-linear rheological behavior of wheat flour dough. *J Food Eng* 100(2):278–288. <https://doi.org/10.1016/j.jfoodeng.2010.04.010>
- Chawla P, DeMan JM, Smith KA (1990) Crystal morphology of shortening and margarines. *Food Struct* 9:329–336
- Cho KS, Hyun K, Ahn KH, Lee SJ (2005) A geometrical interpretation of large amplitude oscillatory shear response. *J Rheol* 49(3):747–758. <https://doi.org/10.1122/1.1895801>
- Dimitriou CJ, Ewoldt RH, McKinley GH (2013) Describing and prescribing the constitutive response of yield stress fluids using large amplitude oscillatory shear stress (LAOStress). *J Rheol* 57(1):27–70. <https://doi.org/10.1122/1.4754023>
- Divoux T, Fardin MA, Manneville S, Lerouge S (2015) Shear banding of complex fluids. *Annu Rev Fluid Mech* 48:81–103
- Ewoldt RH, Bharadwaj NA (2013) Low-dimensional intrinsic material functions for nonlinear viscoelasticity. *Rheol Acta* 52(3):201–219. <https://doi.org/10.1007/s00397-013-0686-6>
- Ewoldt RH, Hosoi AE, McKinley GH (2008) New measures for characterizing nonlinear viscoelasticity in large amplitude oscillatory shear. *J Rheol* 52(6):1427–1458. <https://doi.org/10.1122/1.2970095>
- Ewoldt RH, Hosoi AE, McKinley GH (2009) Nonlinear viscoelastic biomaterials: meaningful characterization and engineering inspiration. *Integr Comp Biol* 49(1):40–50. <https://doi.org/10.1093/icb/icip010>
- Ewoldt RH, Johnston MT, Caretta LM (2015) Experimental challenges of shear rheology : how to avoid bad data. In: Spagnolie SE (ed) *Complex fluids in Biological systems*. Springer, New York, pp 207–241
- Ewoldt RH, McKinley GH (2010) On secondary loops in LAOS via self-intersection of Lissajous–Bowditch curves. *Rheol Acta* 49(2):213–219. <https://doi.org/10.1007/s00397-009-0408-2>
- Ewoldt RH, Winter P, Maxey J, McKinley GH (2010) Large amplitude oscillatory shear of pseudoplastic and elastoviscoplastic materials. *Rheol Acta* 49(2):191–212. <https://doi.org/10.1007/s00397-009-0403-7>
- Faber TJ, Van Breemen LCA, McKinley GH (2017) From firm to fluid-structure-structure-texture relations of filled gels probed under large amplitude oscillatory shear. *J Food Eng* 210:1–18. <https://doi.org/10.1016/j.jfoodeng.2017.03.028>
- Gibaud T, Perge C, Lindström SB, Taberlet N, Manneville S (2016) Multiple yielding processes in a colloidal gel under large amplitude oscillatory stress. *Soft Matter*:1701–1712
- Lin-Gibson S, Pathak JA, Grulke EA, Wang H, Hobbie EK (2004) Elastic flow instability in nanotube suspensions. *Phys Rev Lett* 92(4):048302. <https://doi.org/10.1103/PhysRevLett.92.048302>
- Graham MD (1995) Wall slip and the non-linear dynamics of large amplitude oscillatory shear. *J Rheol* 39(4):697–712. <https://doi.org/10.1122/1.550652>
- Haighton AJ (1965) Worksoftening of margarine and shortening. *J Am Oil Chem Soc* 42(1):27–30. <https://doi.org/10.1007/BF02558248>
- Hammouda B (2010) A new Guinier-Porod model. *J Appl Crystallogr* 43(4):716–719. <https://doi.org/10.1107/S0021889810015773>
- Heertje I (1993) Microstructural studies in fat research. *Food Struct* 12:77–94
- Heertje I, van Eendenburg J, Cornelissen JM, Juriaanse AC (1988) The effect of processing on some microstructural characteristics of fat spreads. *Food Microstruct* 7:189–193
- Hyun K, Kim SH, Ahn KH, Lee SJ (2002) Large amplitude oscillatory shear as a way to classify the complex fluids. *J Nonnewton Fluid Mech* 107(1-3):51–65. [https://doi.org/10.1016/S0377-0257\(02\)00141-6](https://doi.org/10.1016/S0377-0257(02)00141-6)
- Hyun K, Wilhelm M, Klein CO, Cho KS, Nam JG, Ahn KH, Lee SJ, Ewoldt RH, McKinley GH (2011) Progress in polymer science a review of nonlinear oscillatory shear tests : analysis and application of large amplitude oscillatory shear (LAOS). *Prog Polym Sci* 36(12):1697–1753. <https://doi.org/10.1016/j.progpolymsci.2011.02.002>
- Ilavsky J, Allen AJ, Levine LE, Zhang F, Jemian PR, Long GG (2012) High-energy ultra-small-angle X-ray scattering instrument at the advanced photon source. *J Appl Crystallogr* 45(6):1318–1320. <https://doi.org/10.1107/S0021889812040022>
- Ilavsky J, Jemian PR (2009) Irena: tool suite for modeling and analysis of small-angle scattering. *J Appl Crystallogr* 42(2):347–353. <https://doi.org/10.1107/S0021889809002222>
- Ilavsky J, Zhang F, Allen AJ, Levine LE, Jemian PR, Long GG (2013) Ultra-small-angle X-ray scattering instrument at the advanced photon source: history, recent development, and current status. *Metall Mater Trans A* 44(1):68–76. <https://doi.org/10.1007/s11661-012-1431-y>
- Irwin GR (1948) *Fracture dynamics*. In: *Fracturing of metals*. American society of metals, Cleveland, OH, pp 147–166
- Jacob AR, Deshpande AP, Bouteiller L (2014) Large amplitude oscillatory shear of supramolecular materials. *J Nonnewton Fluid Mech* 206:40–56. <https://doi.org/10.1016/j.jnnfm.2014.03.001>
- Kim J, Merger D, Wilhelm M, Helgeson ME (2014) Microstructure and nonlinear signatures of yielding in a heterogeneous colloidal gel under large amplitude oscillatory shear. *J Rheol* 58(5):1359–1390. <https://doi.org/10.1122/1.4882019>
- Kloek W, van Vliet T, Walstra P (2005) Large deformation behavior of fat crystal networks. *J Texture Stud* 36:516–543

- Lake J (1967) An iterative method of slit-correcting small angle X-ray data. *Acta Crystallogr* 23(2):191–194. <https://doi.org/10.1107/S0365110X67002440>
- Laurati M, Egelhaaf SU, Petekidis G (2011) Nonlinear rheology of colloidal gels with intermediate volume fraction. *J Rheol* 55(3):673–706. <https://doi.org/10.1122/1.3571554>
- Li X, Wang SQ, Wang X (2009) Nonlinearity in large amplitude oscillatory shear (LAOS) of different viscoelastic materials. *J Rheol* 53(5):1255–1274. <https://doi.org/10.1122/1.3193713>
- Long GG, Jemian PR, Weertman JR, Black DR, Burdette HE, Spal R (1991) High-resolution small-angle X-ray scattering camera for anomalous scattering. *J Appl Crystallogr* 24(1):30–37. <https://doi.org/10.1107/S0021889890009256>
- Macias-Rodriguez BA, Marangoni AA (2017) Linear and nonlinear rheological behavior of fat crystal networks. *Crit Rev Food Sci Nutr* 8398:0–0
- Macias-Rodriguez BA, Peyronel F, Marangoni AG (2017) The role of nonlinear viscoelasticity on the functionality of laminating shortenings. *J Food Eng*:1–10
- Macias-Rodriguez B, Marangoni AG (2016a) Rheological characterization of triglyceride shortenings. *Rheol Acta* 55(9):767–779. <https://doi.org/10.1007/s00397-016-0951-6>
- Macias-Rodriguez B, Marangoni AG (2016b) Physicochemical and rheological characterization of roll-in shortenings. *J Am Oil Chem Soc* 93(4):575–585. <https://doi.org/10.1007/s11746-016-2792-y>
- Maleky F, Smith AK, Marangoni AG (2011) Laminar shear effects on crystalline alignments and nanostructure of a triacylglycerol crystal network. *Cryst Growth Des* 11(6):2335–2345. <https://doi.org/10.1021/cg200014w>
- Marangoni AG, Acevedo NC, Maleky F, Co E, Peyronel F, Mazzanti G, Quinn B, Pink D (2012) Structure and functionality of edible fats. *Soft Matter* 8(5):1275–1300. <https://doi.org/10.1039/C1SM06234D>
- Min Kim J, Eberle APR, Kate Gurmon A, Porcar L, Wagner NJ (2014) The microstructure and rheology of a model, thixotropic nanoparticle gel under steady shear and large amplitude oscillatory shear (LAOS). *J Rheol* 58(5):1301–1328. <https://doi.org/10.1122/1.4878378>
- Moghimi E, Jacob AR, Koumakis N, Petekidis G (2017) Colloidal gels tuned by oscillatory shear. *Soft Matter* 13(12):2371–2383. <https://doi.org/10.1039/C6SM02508K>
- Narine SS, Marangoni AG (1999a) Mechanical and structural model of fractal networks of fat crystals at low deformations. *Phys Rev E Stat Phys Plasmas Fluids Relat Interdiscip Topics* 60(6 Pt B):6991–7000
- Narine SS, Marangoni AG (1999b) Relating structure of fat crystal networks to mechanical properties. A review *Food Res Int* 32(4):227–248. [https://doi.org/10.1016/S0963-9969\(99\)00078-2](https://doi.org/10.1016/S0963-9969(99)00078-2)
- Narine SS, Marangoni AG (1999c) Fractal nature of fat crystal networks. *Phys Rev E* 59(2):1908–1920. <https://doi.org/10.1103/PhysRevE.59.1908>
- Orowan E (1949) Fracture and strength of solids. *Rep Prog Phys* 12(1):185–232. <https://doi.org/10.1088/0034-4885/12/1/309>
- Peyronel F, Pink DA, Marangoni AG (2014a) Triglyceride nanocrystal aggregation into polycrystalline colloidal networks: ultra-small angle X-ray scattering, models and computer simulation. *Curr Opin Colloid Interface Sci* 19(5):459–470. <https://doi.org/10.1016/j.cocis.2014.07.001>
- Peyronel F, Quinn B, Marangoni AG, Pink DA (2014b) Ultra small angle x-ray scattering in complex mixtures of triacylglycerols. *J Phys Condens Matter* 26(46):464110. <https://doi.org/10.1088/0953-8984/26/46/464110>
- Pink DA, Peyronel F, Quinn B, Singh P, Marangoni AG (2015) Condensation versus diffusion. A spatial-scale-independent theory of aggregate structures in edible oils: applications to model systems and commercial shortenings studied via rheology and USAXS. *J Phys D Appl Phys* 48:384003
- Ramamirtham S, Shahin S, Basavaraj MG, Deshpander AP (2017) Controlling the yield behavior of fat-oil mixtures using cooling rate. *Rheol Acta* 56(12):971–982. <https://doi.org/10.1007/s00397-017-1048-6>
- Ritchie RO (2011) The conflicts between strength and toughness. *Nat Mater* 10(11):817–822. <https://doi.org/10.1038/nmat3115>
- Rogers SA (2012) A sequence of physical processes determined and quantified in (LAOS): an instantaneous local 2D/3D approach. *J Rheol* 56(5):1129–1151. <https://doi.org/10.1122/1.4726083>
- Rogers SA, Erwin BM, Vlassopoulos D, Cloitre M (2011) A sequence of physical processes determined and quantified in LAOS: application to a yield stress fluid. *J Rheol* 55(2):435–458. <https://doi.org/10.1122/1.3544591>
- Rogers SA, Lettinga MP (2012) A sequence of physical processes determined and quantified in large-amplitude oscillatory shear (LAOS): application to theoretical nonlinear models. *J Rheol* 56(1):1–25. <https://doi.org/10.1122/1.3662962>
- Scott Blair GW (1954) The rheology of fats: a review. *J Sci Food Agric* 5(9):401–405. <https://doi.org/10.1002/jsfa.2740050902>
- Sen D, Buehler MJ (2011) Structural hierarchies define toughness and defect-tolerance despite simple and mechanically inferior brittle building blocks. *Sci Rep* 1:1–9
- Sone T (1961) The rheological behavior and thixotropy of a fatty plastic body. *J Phys Soc Japan* 16(5):961–971. <https://doi.org/10.1143/JPSJ.16.961>
- Thareja P (2013) Rheology and microstructure of pastes with crystal network. *Rheol Acta* 52(5):515–527. <https://doi.org/10.1007/s00397-013-0716-4>
- Thomas TY (1961) Plastic flow and fracture in solids. In: Bellman R (ed) *Plastic flow and fracture in solids*. Academic Press, London
- Thomas TY (1967) Slip and fracture in brittle solids. *Int J Eng Sci* 5(8):621–635. [https://doi.org/10.1016/0020-7225\(67\)90061-4](https://doi.org/10.1016/0020-7225(67)90061-4)
- Uauy R, Aro A, Clarke R, Ghafoorunissa R, L'Abbe M, Mozaffarian D, Skeaff M, Stender S, Tavella M (2009) WHO Scientific Update on trans fatty acids: summary and conclusions. *Eur J Clin Nutr* 63:68–75
- van den Tempel M (1961) Mechanical properties of plastic-disperse systems at very small deformations. *J Colloid Sci* 16(3):284–296. [https://doi.org/10.1016/0095-8522\(61\)90005-8](https://doi.org/10.1016/0095-8522(61)90005-8)
- van den Tempel M (1958) Rheology of plastic fats. *Rheol Acta* 1(2-3):115–118. <https://doi.org/10.1007/BF01968849>
- van der Vaart K, Rahmani Y, Zargar R, Hu Z, Bonn D, Schall P (2013) Rheology of concentrated soft and hard-sphere suspensions. *J Rheol* 57(4):1195–1209. <https://doi.org/10.1122/1.4808054>
- Vartiainen E, Laatikainen T, Peltonen M, Juolevi A, Mannisto S, Sundvall J, Jousilahti P, Salomaa V, Valsta L, Puska P (2010) Thirty-five-year trends in cardiovascular risk factors in Finland. *Int J Epidemiol* 39(2):504–518. <https://doi.org/10.1093/ije/dyp330>